International Journal of Coal Science & Technology (2025) 12:96
https://doi.org/10.1007/s40789-025-00826-w

RESEARCH

Evaluation of hydrodynamic forces on offshore wind power piles induced by submarine landslides at various impact depths

Xingsen Guo[1,2,6,7,8] · Xiaolei Liu[1,2,7] · Hong Zhang[3] · Junkai Sun[1,2] · Thianlai Goh[4] · Alessandro Leonardi[5]

Received: 13 August 2024 / Revised: 21 November 2024 / Accepted: 24 July 2025
© The Author(s) 2025

Abstract

The rapid growth of offshore wind farm construction requires reliable pile foundation designs that can withstand complex marine loads. However, current design practices for these foundations often neglect the potential threat of submarine debris flows, which can exert highly destructive forces. This study employs a CFD approach to simulate the effects of submarine debris flows on piles in intricate marine environments, with model accuracy validated against a series of laboratory experiments calculating lateral forces from debris flows. We investigate the impact of debris flows on piles across a range of Reynolds numbers, including variations in rheological properties, density, impact velocity, and initial debris flow heights. Our results reveal that the dominant force exerted by submarine debris flows on piles is primarily a horizontal drag force. We identify three distinct stages in the impact process and emphasize the peak drag force as the critical load on the pile. The study provides a comprehensive analysis of the mechanisms driving variations in drag force and highlights the nonuniform distribution of drag forces along the pile's length. The debris flow height significantly influences not only the magnitude of the peak drag force but also the action point location of this force along the pile. Finally, we propose quantifiable methods for evaluating the peak drag force coefficient and its action point, enhancing the design resilience of pile foundations against submarine debris flows.

Highlights

(1) A CFD approach is proposed and validated for numerically investigating the impact of submarine debris flows on piles in complex marine environments.
(2) The study underscores the primary significance of the drag force in the impact of submarine debris flows on offshore wind turbine piles, especially the peak drag force.
(3) The study reveals that varying debris flow heights can have a substantial impact, resulting in significant differences in peak drag forces, and identifying its action point is highlighted as crucial.
(4) The dynamic interaction between submarine debris flows and piles unveils the mechanism governing the evolution of drag forces under intricate working conditions.
(5) The study provides quantifiable relationships for key parameters, offering practical insights for evaluating the impact of submarine debris flows on piles.

✉ Xiaolei Liu
xiaolei@ouc.edu.cn

Xingsen Guo
xingsen.guo@ouc.edu.cn

Hong Zhang
zhanghong9645@ouc.edu.cn

Junkai Sun
sunjunkai@stu.ouc.edu.cn

Thianlai Goh
gdsbgoh@gmail.com

Alessandro Leonardi
a.leonardi@sheffield.ac.uk

[1] Shandong Provincial Key Laboratory of Marine Engineering Geology and the Environment, Ocean University of China, Qingdao 266100, China

[2] Department of Civil, Environmental and Geomatic Engineering, University College London, London WC1E 6BT, United Kingdom

[3] College of Engineering, Ocean University of China, Qingdao 266100, China

[4] Program Geology, Faculty of Science and Technology, Universiti Kebangsaan Malaysia, Bangi 43600, Malaysia

[5] Department of Civil and Structural Engineering, University of Sheffield, Sheffield S1 3JD, United Kingdom

[6] Department of Engineering, University of Cambridge, Cambridge CB2 1PZ, United Kingdom

[7] Sanya Oceanographic Institution, Ocean University of China, Sanya 572024, China

[8] State Key Laboratory of Ocean Engineering, Shanghai Jiao Tong University, Shanghai 200240, China

Published online: 21 November 2025

Keywords Submarine debris flow · Offshore wind turbine pile · CFD modelling · Drag force · Impact height

1 Introduction

As a crucial component of renewable energy, offshore wind power is gradually becoming a cornerstone in the global energy transition (International Energy Agency 2021; Melissas and Asprogerakas 2022; Wu et al. 2024a). In comparison to onshore wind power, offshore wind farms possess advantages such as high energy density, stable supply, and reduced environmental impact. However, offshore wind farms located far from the shore must endure harsh marine environments, resulting in construction and operational costs significantly higher than those of fossil fuel and onshore wind power. Thus, cost-effectiveness becomes a critical factor affecting these developments. The foundation costs of wind turbines account for a substantial proportion, ranging from 20 to 30%, of the total cost of offshore wind power (Byrne et al. 2002; Wang et al. 2017). Foundation instability can easily lead to the failure of a wind turbine, leading to heavy financial losses.

To adapt to different water depths and seabed geological conditions, the offshore wind power industry has developed two types of turbines: fixed and floating (Lai et al. 2024; Xu et al. 2025). The technology for floating wind turbines is still undergoing development. Therefore, fixed type is still the most common design (Kirkwood 2016). The main types of foundations for fixed turbines are gravity types, large-diameter monopiles, pile groups, single tubes, and multi-tube foundations (Miceli 2012; Faizi et al. 2019; Wu et al. 2019; Zhao et al. 2023). The monopile, which is suitable for water depths ranging from 0 to 40 m, is the mainstream choice, and as of 2019 was used for over 80% of installations in Europe (Wind Europe 2020). Despite their popularity, the construction and long-term operation of monopile-based turbines face complex challenges due to uncertainties in the seabed geological environment and marine dynamics (Feng et al. 2019; Gao and Yin 2022; Yu et al. 2022; Liu et al. 2023; Rui et al. 2024).

A typical design process for monopiles considers wind loads, wave loads, tidal currents, seismic loads, ice loads, self-weight loads, and temperature loads, but loads from potential geohazards are often overlooked, due to the multiple uncertainties. Figure 1a illustrates the global distribution of offshore wind power sites and the susceptibility to submarine landslides (Obelcz et al. 2019; Dunnett et al. 2020). Offshore wind farms are often situated in regions susceptible to submarine landslides. In addition, the rising frequency of extreme storm events in recent years (Shi et al. 2024; Dai and Nie 2022) has heightened the risk of submarine debris flows triggered by seabed liquefaction, posing a growing threat to wind turbine foundations (Du et al. 2020; Taftsoglou et al. 2022). This increasing risk is primarily driven by the rapid geographic expansion of offshore wind farms, coupled with the exponential growth in the number of wind turbines worldwide. This is problematic because submarine landslides can have a significant impact, generating loads that may exceed the design capacity of the monopile, leading to potential instability and overturning (Fig. 1b). Thus, further research is urgently required to develop models capable of quantitatively assessing the impact of submarine landslides on wind turbine piles.

Submarine debris flow is often generated from landslides, originating from the rapid sliding of unconsolidated sediments or sediments with weak structural planes along a sloping seabed. In a broad sense, this concept also encompasses various sediment transport processes on the seabed, such as mud flows, liquefaction flows, and turbidity currents (Locat and Lee 2002; Hance 2003; Shan et al. 2022; Sørlie et al. 2023; Guo et al. 2023). Debris flows and turbidity currents, which often develop in the late stages of submarine landslide

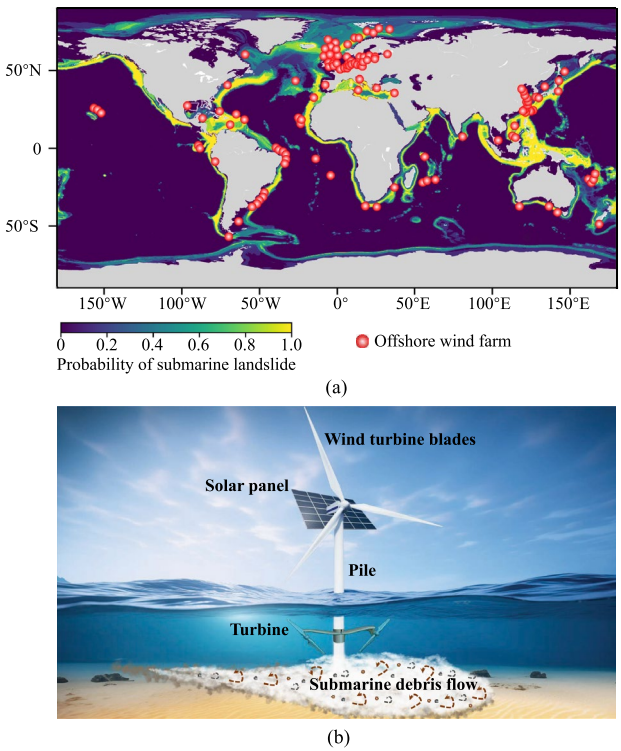

Fig. 1 **a** Global distribution of offshore wind power sites and the susceptibility to submarine landslides (Obelcz et al. 2019; Dunnett et al. 2020); **b** Conceptual diagram of a pile foundation impacted by a submarine debris flow

mass evolution, have been the focus of recent literature (Hsu et al. 2008; Zakeri et al. 2012 and 2013; Guo et al. 2022). This is due to the high velocities that these phenomena can reach, which potentially lead to significant impacts on marine structures. Many researchers have examined the impact of submarine debris/mud flows on pipeline and cable systems with high aspect ratios, employing methods such as flume experiments, centrifuge tests, and numerical simulations (Wang et al. 2008; Zakeri et al. 2008 and 2009; Haza et al. 2013; Liu et al. 2015; Dong et al. 2017; Wang et al. 2018; Wang et al. 2024; Guo et al. 2024a; Wu et al. 2024b). Notwithstanding the complexity of these models, plane-strain conditions are often assumed, simplifying the problem effectively to 2D, and neglecting the effects in the axis parallel to the pipeline. In this context, computational fluid dynamics (CFD) methods are often employed, and empirical equations to calculate the impact loads have been proposed (Sahdi et al. 2019; Qian et al. 2020; Fan et al. 2018).

The lack of validation data from field case studies has motivated the need for scaled laboratory experiments. For example, Feng et al. (2019) conducted flume experiments to analyze the impact forces of submarine debris flows on monopiles at varying Reynolds numbers. However, the empirical assessment equation established in this study did not account for the influence of impact height and the action position (i.e., the action point) of submarine debris flows, making its practical application challenging. In a similar vein, Sørlie et al. (2023) also conducted flume experiments on clay-rich submarine mud flows, revealing a hydroplaning mechanism, and shedding light on the impact forces on monopiles subject to geohazards. These studies highlight how the impact of submarine debris or mud flows on monopiles represents a fully three-dimensional problem of high complexity. In contrast to experimental studies, numerical simulations offer several advantages, including cost-effectiveness, controllable conditions, high time efficiency, excellent repeatability, flexibility in exploring scale effects and parameters, and suitability for isolating elusive mechanistic phenomena. Li et al. (2021) carried out research on the impact forces of submarine debris flows on piles using a CFD method. It is apparent that this intricate impact scenario might result in nonuniform impact forces on the pile, highlighting the significance of assessing force action points—an essential aspect that has been previously overlooked. Hence, there is an urgent need for an effective numerical simulation method that can replicate the three-dimensional transient impact processes of submarine debris or mud flows on piles, quantify the potential risk associated with impact forces and their action points for enhancing foundation design to improve the resistance and stability of wind turbine pile foundations.

This study employs a CFD approach using an incompressible two-phase flow model to simulate the impact of submarine debris flows. In this approach, the Herschel-Bulkley rheological model is utilized, and the accuracy of the numerical model is validated by the results of laboratory experiments, focusing on the recorded impact loads. Based on this, we comprehensively simulate and analyze complex scenarios, particularly regarding varying impact heights. The findings of this study provide valuable insights in assessing the impact of submarine debris or mud flows on offshore wind turbine piles, offering a basis for evaluating the vulnerability of offshore wind turbine foundations to potential submarine geohazards.

2 Methodology

2.1 Numerical framework

When investigating the instantaneous impact of submarine debris flows on offshore wind power piles, a reasonable approach is to simplify the submarine debris flow as a uniform non-Newtonian fluid. In this study, we employ a Herschel-Bulkley model (Guo et al. 2023; Zhu et al. 2020), characterized by shear thinning with a laminar flow pattern. Similarly, seawater is also simplified as a uniform Newtonian fluid, with turbulent effects simulated using a k-ε model. Given the brief duration of impact, this study disregards mass transfer between submarine debris flows and seawater. This simplification streamlines transient impact simulations and enhances accuracy by excluding uncertainties from variations in mixed fluid density and viscosity due to the interaction between submarine debris flow and seawater, where the changes in physical and mechanical parameters of the mixed fluid are nonlinear. To simulate the motion of submarine debris flows within seawater, the CFD multiphase flow model employs a free-surface flow approach. The monopile is simplified as a fixed boundary, allowing for an exploration of the complete fluid dynamics of both substances and their interaction with this boundary. In this context, the submarine debris flow is represented as phase α while the surrounding seawater is denoted as β. The utilized two-phase free surface flow model is categorized as an inhomogeneous model (CFX 2020a and 2020b). In the inhomogeneous model, the interaction of phases α and β occurs through the momentum transfer term. Specifically, phase α and phase β possess distinct properties and flow parameters such viscosity and density, but the pressure field is uniform across the two phases (Guo et al. 2024b). The volume fraction of each phase is designated as r, and $\sum_{\alpha=1}^{N_P} r_\alpha = 1$, with the total number of phases N_P=2. The governing equations, encompassing mass and momentum conservation, are outlined from Eq. (1) to Eq. (4):

$$\begin{cases} \dfrac{\partial}{\partial t}\left(r_\alpha \rho_\alpha\right) = 0 \\ \dfrac{\partial}{\partial t}\left(r_\beta \rho_\beta\right) = 0 \end{cases} \tag{1}$$

where ρ is the (constant) density of each phases.

$$\begin{cases} \frac{\partial}{\partial t}\left(r_\alpha \rho_\alpha U_\alpha\right) + \nabla \cdot \left(r_\alpha\left(\rho_\alpha U_\alpha \otimes U_\alpha\right)\right) = -r_\alpha \nabla P_\alpha + \nabla \cdot \left(r_\alpha \mu_\alpha\left(\nabla U_\alpha + \left(\nabla U_\alpha\right)^{\mathrm{T}}\right)\right) + S_{M\alpha} + M_\alpha^D \\ \frac{\partial}{\partial t}\left(r_\beta \rho_\beta U_\beta\right) + \nabla \cdot \left(r_\beta\left(\rho_\beta U_\beta \otimes U_\beta\right)\right) = -r_\beta \nabla P_\beta + \nabla \cdot \left(r_\beta \mu_\beta\left(\nabla U_\beta + \left(\nabla U_\beta\right)^{\mathrm{T}}\right)\right) + S_{M\beta} + M_\beta^D \end{cases} \tag{2}$$

where P and U are pressure and velocity; μ is the viscosity; S_{M} is the buoyancy momentum source caused by the difference between the phase densities, and refers to gravity; and M^D is the interphase drag force.

$$\begin{cases} S_{M\alpha} = (\rho_\alpha - \rho_\beta) \times g \\ S_{M\beta} = (\rho_\beta - \rho_\beta) \times g = 0 \end{cases} \tag{3}$$

where g is the gravitational acceleration.

$$M_\alpha^D = -M_\beta^D = \frac{1}{2}\rho_\beta C_D A_\alpha (U_\alpha - U_\beta)\left|U_\alpha - U_\beta\right| \tag{4}$$

where C_D is the drag coefficient, which is taken as 2.0 (Zakeri et al. 2009; Fan et al. 2018; Qian et al. 2020); and A_α is the interface area, which is calculated as $A_\alpha = \left|\nabla r_\alpha\right|$.

2.2 Validation from CFD simulation case: time-dependent impact forces on the pipe

To validate the reliability of our numerical modelling, this study simulated the impact of a submarine slide mass on a suspended pipe, utilizing a CFD result (Fan et al. 2018). Figure 2a illustrates the generalized model of the submarine slide mass on the suspended pipe, encompassing both geometry and boundary conditions. Specifically, the density of the submarine slide mass is set to 1681 kg/m^3, and its shear behavior is described by the Herschel-Bulkley rheological model of $\tau = 7.3 + 3\dot{\gamma}^{0.35}$ Pa (Zakeri et al. 2008). The diameter of the suspended pipe is $D = 25$ mm, and its simulation incorporates the no-slip boundary condition (Fan et al. 2018). The density of ambient water is set to 997 kg/m^3. Initially, the submarine slide mass moves to the right from the inlet at an initial velocity of 0.93 m/s (Fan et al. 2018), impacting the fixed pipe. For this case, the minimum grid size is set at $0.01D$, with a total grid count of 0.3 million, a total simulation time of 2 s, and a time step (denoted as $\Delta t = l_{\min}/U$, where $l_{\min}$ is the minimum mesh size) of 0.001 s. Additional parameters necessary for the CFD simulation are presented in Table 1. Figure 2b displays the impact force–time history curves obtained by the CFD results from Fan et al. (2018) and our study. In comparison with the previous numerical simulation results (Fan et al. 2018), our numerical simulation demonstrates a remarkable consistency in both the temporal evolution and peak/stable-state values of impact forces, i.e., drag force and lift force. This consistency affirms the accuracy of our CFD numerical modelling.

2.3 Validation from flume experiment case: Peak impact force on the pile

This study uses the flume experiment conducted by Feng et al. (2019) for validation. They simulated submarine debris flows with different proportions of clay, sand, and water, using a Herschel-Bulkley rheological model to describe the flow rheology, as shown in Table 2. Meanwhile, a flume experiment box was used to control the velocities of the

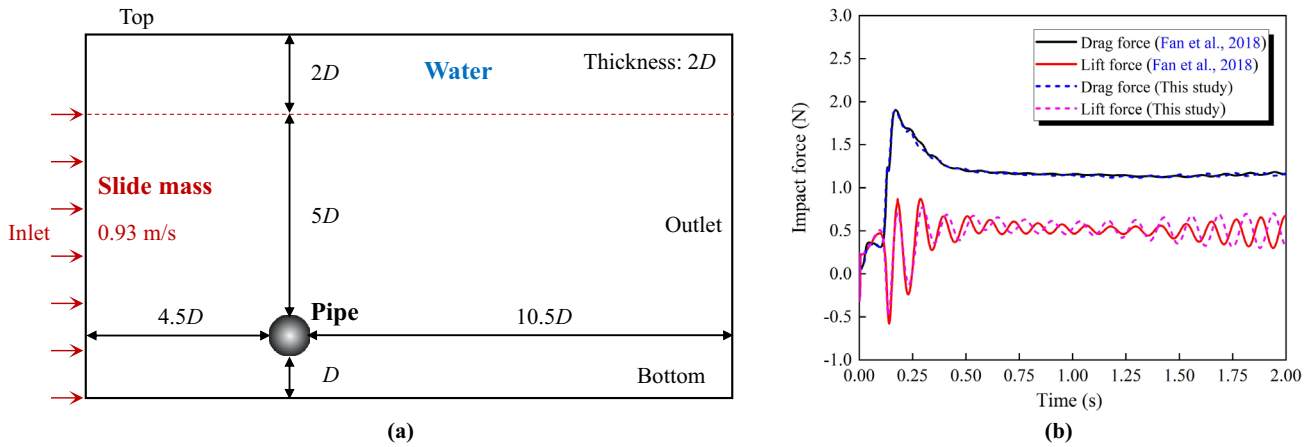

Fig. 2 Investigation of the submarine slide mass impact on the suspended pipe. **a** Generalized model; **b** Impact force–time history curves obtained by the CFD result from Fan et al. (2018) and this study

Table 1 CFD numerical modelling (a case for the impact of a submarine slide mass on a suspended pipe) options and parameters for the computational domain, boundary conditions, and solver control

Option		Parameter
Computational domain	Multiphase model	Incompressible two-phase flow model; Free surface flow model
	Water	Eulerian material, Continuous fluid; Laminar model; Dynamic viscosity: 0.00089 Pa·s; Density: 997 kg/m^3
	Submarine slide mass	Eulerian material, Continuous fluid; Laminar model
	Buoyancy reference density	997 kg/m^3
	Fluid pair model	Momentum transfer, Drag coefficient 2.0
Boundary condition	Top	Free slip wall
	Inlet	0.93 m/s (submarine slide mass)
	Front	Free slip wall
	Back	Free slip wall
	Outlet	Opening
	Bottom	No slip wall
	Pipe	No slip wall
Solver control	Analysis type	Transient
	Advection scheme	High resolution
	Transient scheme	Second order backward Euler
	Convergence control	Min. Coeff. Loops: 1; Max. Coeff. Loops: 50
	Convergence criteria	Root mean square (RMS): 0.00005

submarine debris flows, with different sensors assessing the impact force on the pile. To simplify the analysis and numerical calculations, we selected the key region of interaction between the submarine debris flow and the pile for CFD modelling. Figure 3 presents the geometry and grids for this validation case. The maximum grid size in the CFD domain is 8 mm, and the grid is refined around the pile, with a minimum grid size of 1.5 mm. A total of 10 layers of boundary layer grids are placed on the surface and bottom of the pile, with a total thickness of 2 mm and a growth ratio of 1.20. After conducting the sensitivity analysis, the final total number of nodes for this validation case is approximately 1.4 million, with the total number of elements reaching around 7 million. The finite volume method implemented in ANSYS CFX is employed to solve the conservation equations, Eqs. (1)–(4), and obtain pressure, velocity, and other relevant field variables. This computation process is parallelized through the utilization of a message-passing interface (MPI) platform. For the simulation process, a transient approach is adopted, and the chosen solution mode is a high-resolution second-order backward Euler method. The convergence scheme utilizes the default root mean square for residual assessment, with a specific convergence value set at 0.00005. Table 3 presents the CFD numerical modelling options and parameters for the computational domain, boundary conditions, and solver control.

$$\mu_\alpha = \frac{\tau}{\dot{\gamma}} = \frac{\tau_y + K\dot{\gamma}^n}{\dot{\gamma}} \tag{5}$$

where τ is the shear stress (Pa); τ_y is the yield stress (Pa); K is the consistency factor (Pa·s^n); n is the fluidity index; and $\dot{\gamma}$ is the shear rate (s^{-1}), which can be determined by calculating the ratio of the velocity of the debris flow to the pile diameter.

Table 2 Physical and mechanical parameters of submarine debris flows (Feng et al. 2019)

No.	Mass fraction of materials (%)			Density ρ (kg/m^3)	Rheological model $\tau = \tau_y + K\dot{\gamma}^n$		
	Clay	Sand	Water		Yield stress τ_y (Pa)	Consistency factor K (Pa·s^n)	Fluidity index n
R1	15	50	35	1763	0.5	1.5	0.42
R2	20	45	35	1774	1.8	1.4	0.54
R3	30	35	35	1796	5.9	0.9	0.87

The dynamic viscosity of a submarine debris flow is described by the Herschel-Bulkley rheological model as follows:

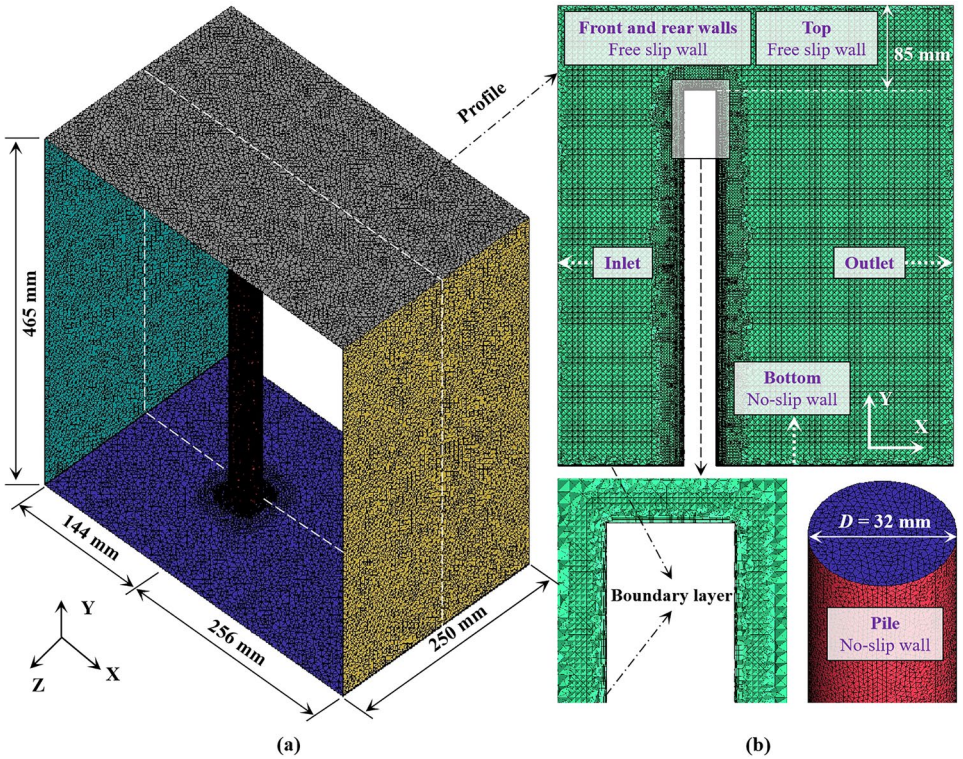

Fig. 3 Geometry and grids of the validation cases for the flume experiment of a pile impacted by submarine debris flows. **a** Overall visualisation; **b** Local visualisation

Table 3 CFD numerical modelling (pile) options and parameters for the computational domain, boundary conditions, and solver control

Option		Parameter
Computational domain	Multiphase model	The same as in Table 1
	Water	Eulerian material, Continuous fluid; *k-ε* turbulence model Density: 997 kg/m^3; Dynamic viscosity: 0.00089 Pa·s
	Submarine debris flow	The same as in Table 1
	Buoyancy reference density	The same as in Table 1
	Fluid pair model	The same as in Table 1
Boundary condition	Top	The same as in Table 1
	Inlet	Impact velocity of the submarine landslide
	Front	The same as in Table 1
	Back	
	Outlet	
	Bottom	
	Pile	No slip wall
Solver control	The same as in Table 1	

This study simulates two cases with Reynolds numbers of 230 and 160, respectively, and also varying the debris flow height (23.8 cm and 22.6 cm) and impact velocity (0.94 m/s and 0.75 m/s), as shown in Table 4. The total duration for these simulated cases is 2 s, with a time step ($\Delta t = l_{\min}/U$) of 0.001 s. Figure 4 presents the experimental and numerical result comparisons of peak horizontal impact forces under different submarine debris flow height conditions. In the numerical simulation results, the horizontal impact force on the pile rapidly increases with time, reaching a peak and then decreasing to a stable impact load. The simulation results show that the horizontal impact force also increases with increasing submarine debris flow impact height. Under the same submarine debris flow impact height conditions, the peak horizontal impact force obtained from the CFD numerical modelling established in this study closely matches the experimental results from Feng et al. (2019). This demonstrates that the CFD numerical modelling developed in this study can effectively assess the impact load of submarine

Table 4 Specific parameters of validation cases

Case	Impact height in the simulation H_{peak} (cm)	Impact height in the experiment (cm)	Rheological model	U (m/s)	Reynolds number Re
1–1	23.9	23.8	R1	0.94	230
1–2	24.4				
1–3	24.9				
2–1	21.6	22.6	R1	0.75	160
2–2	22.3				
2–3	22.5				

debris flows on piles. Figure 5 shows the visualization of the interface between the submarine debris flow and water using submarine debris flow velocity at the moment of peak impact force ($t = 0.37$ s). It can be observed that initially, the submarine debris flow surges in front of the pile, causing a significant difference in the submarine debris flow height in front of and behind the pile. Therefore, when assessing the impact force of submarine debris flows on piles, the impact height of the submarine debris flow is a crucial factor that needs to be considered.

3 Results and discussion

3.1 Set up

To analyze the impact forces of submarine debris flows with varying heights, this study establishes a generalized geometry model as depicted in Fig. 6, with a pile diameter of 25 mm. The grid for this CFD modelling follows the same method as described in Sect. 2.2, with a maximum grid size of 8 mm and refinement of the grid around the pile. The minimum grid size l_{min} is set to 1 mm. Additionally, a boundary layer grid of ten layers is applied adjacent to the pile surface and the bottom boundary, with a total thickness of 2 mm and a growth ratio of 1.20. After conducting grid sensitivity analysis, the final simulation case for this study had a total of approximately 1 million nodes and 4.7 million elements. Various rheological parameters are explored in this study, as shown in Table 2. Different impact heights of submarine debris flows are achieved by defining the initial height (H_0) of the submarine debris flow at the inlet. Furthermore, this study considers different impact velocities. Therefore, the simulation cases in this study involve seven Reynolds numbers, ranging from approximately 9–700. Table 5 provides detailed parameters for the analysis cases. It is worth noting that the time steps and the total simulation time for these cases are determined based on the impact velocity of the

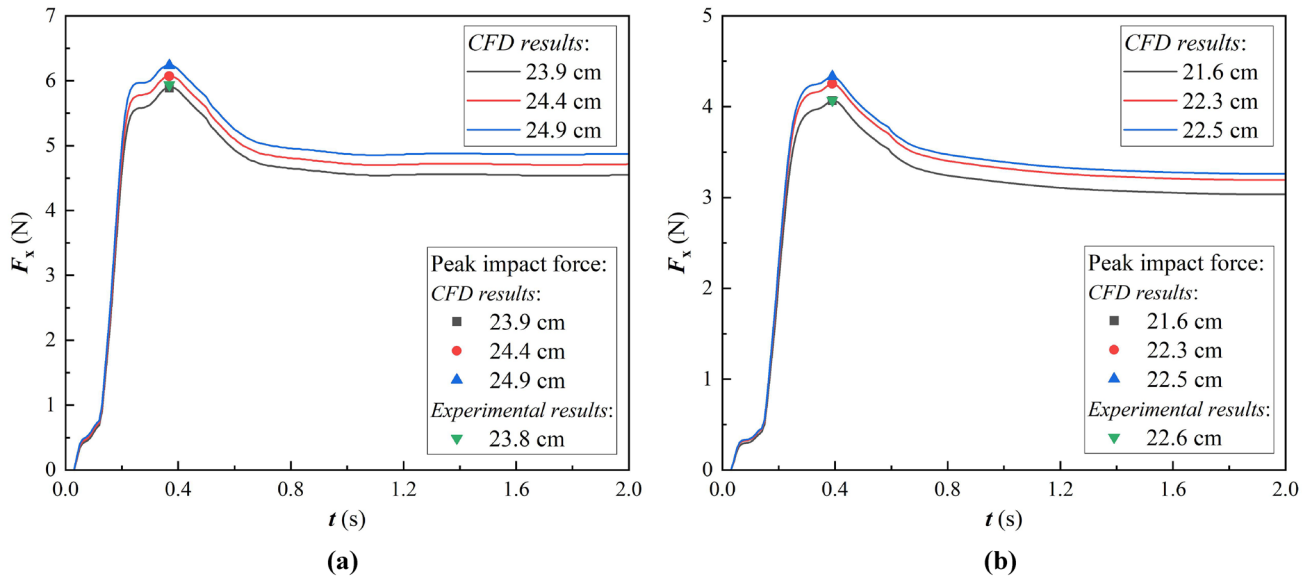

Fig. 4 Experimental and numerical result comparisons of horizontal impact force as a function of time under different submarine debris flow height conditions. **a** Case 1–1; **b** Case 2–3

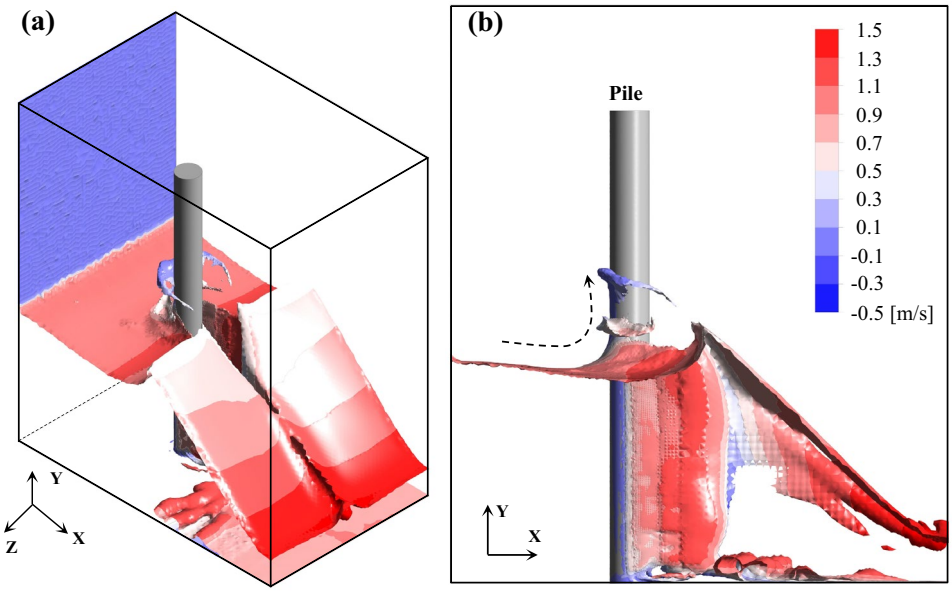

Fig. 5 Visualization of the interface between the submarine debris flow and water using submarine debris flow velocity at the moment of peak impact force $t = 0.37$ s. **a** 3D view; **b** Cross-sectional view

submarine debris flows and the minimum grid size. The settings for other specific simulation parameters and boundary conditions are presented in Fig. 7 and Table 3.

3.2 Impact forces on the pile

Figures 7 and 8 illustrate the duration traces of impact forces (i.e., drag and lift forces) on the pile under different Reynolds numbers for various initial heights of submarine debris flows. First, it can be observed that the impact forces on the pile are primarily horizontal drag forces. In the generalized conditions in this study, the vertical peak lift force accounts for only 2.1%–6.3% of the peak horizontal drag force, indicating that the drag force should be the primary focus when considering the impact of submarine debris flows on the pile. Meanwhile, the duration traces of the drag force exhibit different patterns under different Reynolds number conditions. When the Reynolds number is relatively small, there is little difference between the peak and stable values of the drag force, and no significant peaks are observed, as shown in Fig. 7a. As the Reynolds number increases, the drag force initially increases, then decreases, and eventually stabilizes over time, showing clear peaks. Figure 9 illustrates the difference between the peak and stable drag forces under different conditions of Reynolds number and submarine debris flow impact height. In the generalized conditions, the peak drag force ($F_{\text{D-peak}}$) can be as much as 1.6 times the stable drag force ($F_{\text{D-stable}}$). Therefore, the impact of submarine debris flows on the pile should primarily focus on the peak drag force load. Furthermore, the maximum height (H_{peak}) at which submarine debris flow acts on the pile at the moment of peak drag force is extracted for different cases, as shown in Table 5. In general, the rheological models, the initial

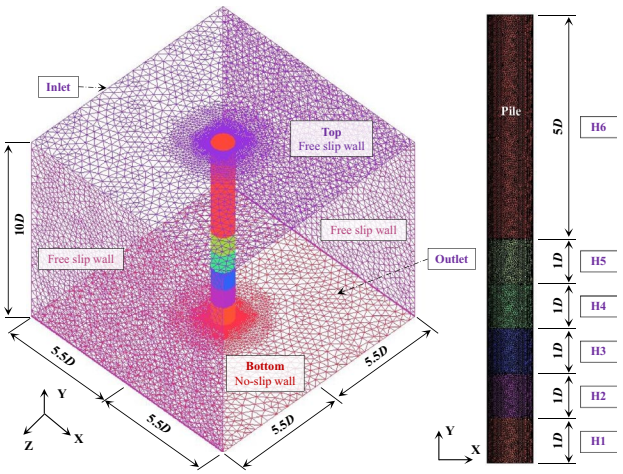

Fig. 6 Geometry and grid information of the analysis cases. Dimensions are scaled by the pile diameter D

heights, and the velocity of submarine debris flows affect the maximum height (H_{peak}) of the submarine debris flow along the pile. With the same rheological model and initial height (H_0) conditions, a higher velocity of submarine debris flow results in a larger H_{peak}. It can be observed that the drag force on the pile (Fig. 7) significantly increases with the initial height of the submarine debris flow. Figure 10 demonstrates the effect of initial height on the peak drag force under different Reynolds number conditions. In the generalized conditions, the effect of the initial height of submarine debris flows on the peak drag force can reach up to 241%.

Table 5 Detailed parameters of the analyzed cases

Case	H_0 (m)	H_{peak} (m)	Rheological model	U (m/s)	Reynolds number Re	Time step (s) l_{min}/U	Total time (s)
1D-1	0.025	0.04915	R3	0.25	9	0.004	10
1D-2		0.06656		0.5	25	0.002	5
1D-3		0.08619		1	64	0.001	2.5
1D-4		0.07582	R2	0.8	100	0.00125	3.125
1D-5		0.09033		1.25	210	0.0008	2
1D-6		0.08975	R1	1.5	450	0.000667	1.667
1D-7		0.09154		2	710	0.0005	1.25
2D-1	0.05	0.06742	R3	0.25	9	0.004	10
2D-2		0.08008		0.5	25	0.002	5
2D-3		0.11336		1	64	0.001	2.5
2D-4		0.103398	R2	0.8	100	0.00125	3.125
2D-5		0.12027		1.25	210	0.0008	2
2D-6		0.11892	R1	1.5	450	0.000667	1.667
2D-7		0.12014		2	710	0.0005	1.25
3D-1	0.075	0.08192	R3	0.25	9	0.004	10
3D-2		0.09648		0.5	25	0.002	5
3D-3		0.13910		1	64	0.001	2.5
3D-4		0.12938	R2	0.8	100	0.00125	3.125
3D-5		0.14544		1.25	210	0.0008	2
3D-6		0.14738	R1	1.5	450	0.000667	1.667
3D-7		0.14626		2	710	0.0005	1.25

3.3 Mechanism discussion

The process of a submarine debris flow impacting a pile can be divided into three stages, as shown in Figs. 7, 11, and 12. In the first stage (Stage I), the submarine debris flow moves forward at its initial height (H_0). When the submarine debris flow begins to make contact with the pile, it rapidly accumulates in front of the pile (on the upstream side) and climbs to its maximum height (H_{peak}) at the front of the pile. At this point, the pressure difference between the front and back of the pile reaches its maximum, creating the peak horizontal impact force on the pile. In the second stage (Stage II), as the submarine debris flow moves further along the pile, the accumulation behind the pile (on the downstream side) increases. The height difference of debris flow between the front and back gradually decreases, leading to a reduction in the pressure difference between the front and back of the pile. This leads to a gradual decrease in the horizontal drag force of the submarine debris flow on the pile. In the third stage (Stage III), as the accumulation in front of the pile diminishes, and the accumulation behind the pile increases, a stable height difference is reached between the front and back of the pile. The pressure difference stabilizes, resulting in the horizontal drag force reaching a steady state. The differences in drag force mechanisms resulting from various Reynolds numbers are primarily reflected in the three generalized processes of submarine debris flow disturbance around the pile as described earlier. At low Reynolds number conditions, Stage II may be absent. Low Reynolds numbers correspond to relatively small submarine debris flow impact velocities, and the submarine debris flow gradually envelops the pile, leading to a slow transition from Stage I to Stage III. In other words, there is no significant change in the accumulation of submarine debris flow on the upstream and downstream sides (front and back) between Stages II and III. This resembles the impact mechanism of submarine debris flows on pipelines under low Reynolds number conditions (Sahdi et al. 2019).

The significant difference in drag force and lift force mentioned above may be largely attributed to the modelling choices of this study. The CFD model assumes that the impact velocity of the submarine debris flow is limited in the horizontal direction. During the simulation of submarine debris flow motion, the vertical velocity of the submarine debris flow is negligible, resulting in minimal lift force acting on the pile. In future research involving more complex conditions, such as seabed sites with varying slopes, the influence of the lift force might have to be reassessed. The differences in peak drag forces on the pile resulting from varying initial heights are evidently influenced by changes in the flow field within the impact range of the submarine debris flow. Taking Reynolds number 210 as an example, Fig. 13 illustrates the duration traces of drag forces on different pile units (see Fig. 6) for Cases 1D-5, 2D-5, and 3D-5

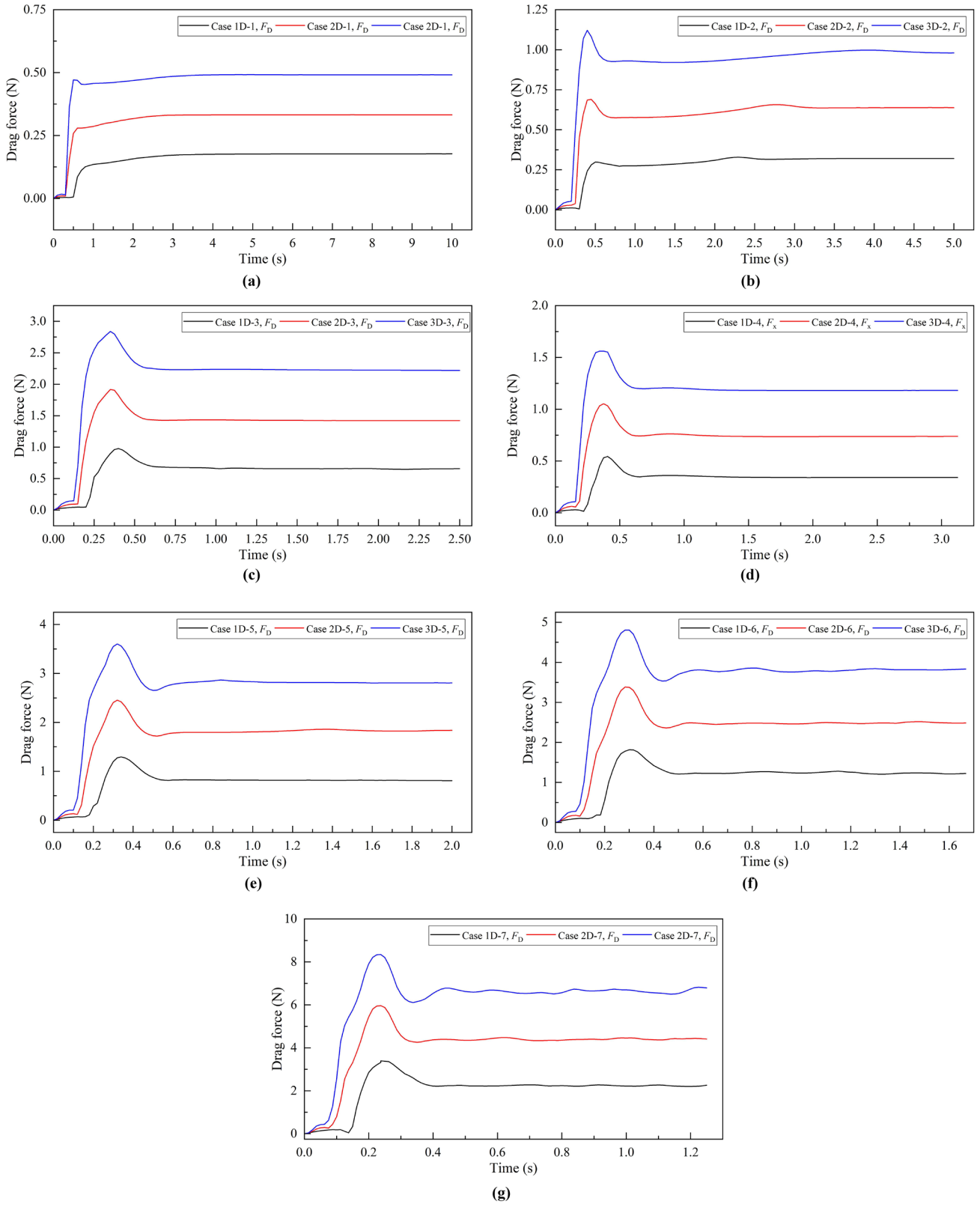

Fig. 7 Duration traces of the drag force on the pile under different impact heights of debris flows. **a** Re = 9; **b** Re = 25; **c** Re = 64; **d** Re = 100; **e** Re = 210; **f** Re = 450; **g** Re = 710

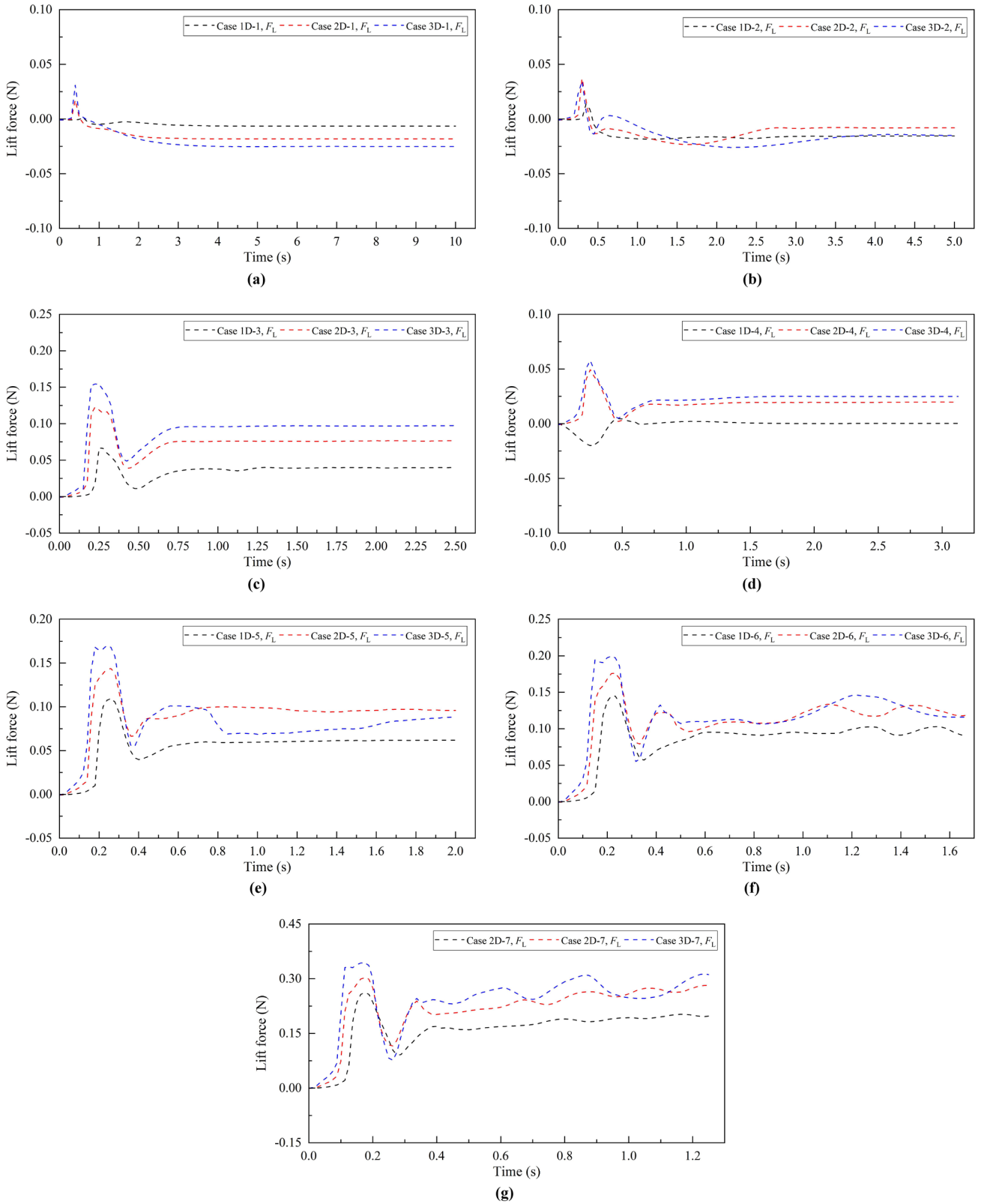

Fig. 8 Duration traces of the lift force on the pile under different impact heights of submarine debris flows: **a** Re = 9; **b** Re = 25; **c** Re = 64; **d** Re = 100; **e** Re = 210; **f** Re = 450; **g** Re = 710

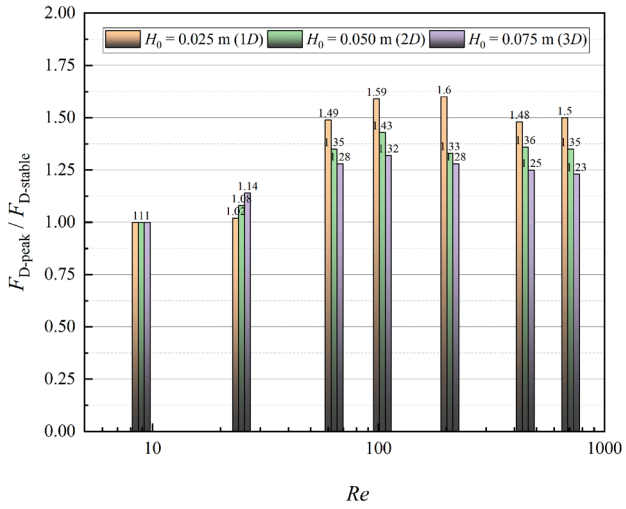

Fig. 9 Effect of peak and stable drag forces of submarine debris flows on piles under different conditions of Reynolds number and impact height

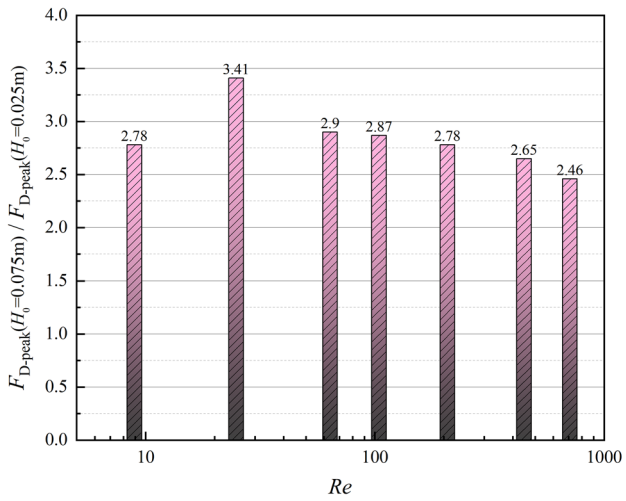

Fig. 10 Effect of impact heights (i.e., H_0 = 0.025 m and H_0 = 0.075 m) of submarine debris flows on peak drag force acting on piles under different Reynolds number conditions

under the same conditions of submarine debris flow initial height. There are significant differences in the drag forces acting on different positions of the pile. For Case 1D-5, the drag force is highest in the H1 unit, followed by a significant decrease in the H2 and H3 units, and negligible force in the H4, H5, and H6 units. For Case 2D-5, the drag force is highest in the H1 unit, followed by gradually decreasing forces in the H2, H3, and H4 units, and negligible forces in the H5 and H6 units. For Case 3D-5, the drag force is highest in the H2 unit, followed by nearly equal forces in the H1 and H3 units, and gradually decreasing forces in the H4 and H5 units, with the lowest force in the H6 unit. Clearly, the impact areas and distribution of forces on the pile show significant differences depending on the flow height, and the drag forces are nonuniformly distributed along the surface of the pile, as shown in Fig. 14a. The differences in the H1 units are mainly due to the slightly earlier-occurring peak, and slight increases in drag force as the initial height of the submarine debris flow increases. This is because a thicker submarine debris flow results in a more pronounced gravitational collapse effect, leading to a slight increase in velocity (Guo et al. 2022). At this moment, the maximum horizontal velocity for Case 1D-5 is 1.33 m/s, for Case 2D-5 is 1.333 m/s, and for Case 3D-5 is 1.335 m/s. There are also differences in the backflow degree of the submarine debris flow, as shown in Fig. 14b. More importantly, submarine debris flows with different initial heights exhibit significant differences in the distribution of velocity fields and density fields around the pile. This results in variations in the drag forces of the H2 and H3 units. Specifically, submarine debris flows with different initial heights impact the pile unevenly and have distinct distributions in different units of the pile, as shown in Fig. 14c.

3.4 Quantitative evaluation

If unavoidable impacts occur, the influence of submarine debris flow loads should be thoroughly assessed. Based on the analysis, the impact load of submarine debris flows on the pile is influenced by the Reynolds number, the velocity and density of the debris flow, and the impact area on the pile (characterized by the initial flow height and pile diameter). Furthermore, it is crucial to note that the drag force of submarine debris flows on the pile is nonuniformly distributed along the pile body, as shown in Fig. 13. Therefore, an evaluation of the action point of the drag force is of paramount importance. Using the data from Figs. 7 and 8 and Table 5, the peak drag force coefficient is calculated based on Eq. (6):

$$C_{\text{D - peak}} = \frac{2F_{\text{D - peak}}}{\rho \cdot U^2 \cdot (D \cdot H_{\text{peak}})} \tag{6}$$

where $C_{\text{D-peak}}$ is the peak drag force coefficient on the pile; $F_{\text{D-peak}}$ is the peak drag force on the pile; and U is the free-flow velocity of the submarine debris flow. The results are shown in Fig. 15. Results show that the drag force coefficient decreases as the Reynolds number increases, eventually stabilizing. Furthermore, by simplifying the drag forces acting on each pile unit immersed under the submarine debris flow as uniform distributions and considering the partially submerged sections of the pile unit that are not fully submerged under the debris flow as uniform distributions, the action point of the peak drag force exerted by the submarine debris flow was calculated as shown in Fig. 16. In terms of the

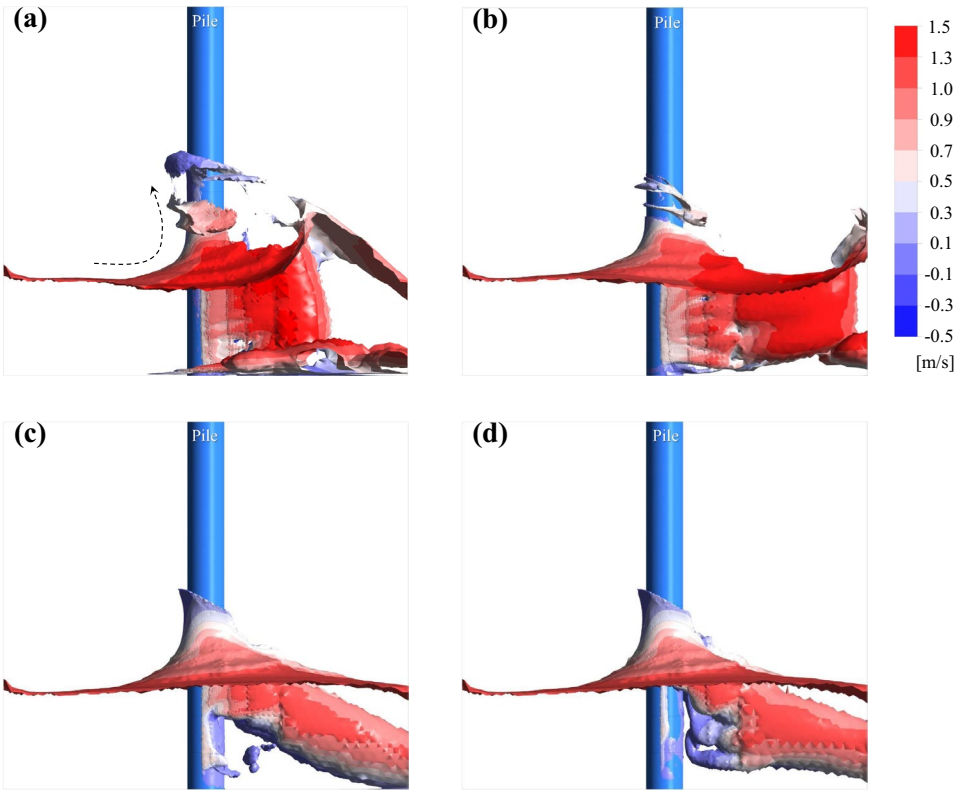

Fig. 11 Visualization of the interface between submarine debris flow and water using submarine debris flow velocity in Case 3D-5. **a** at $t=0.32$ s in Stage I; **b** at $t=0.4$ s in Stage II; **c** at $t=1$ s in Stage III; **d** at $t=2$ s in Stage III

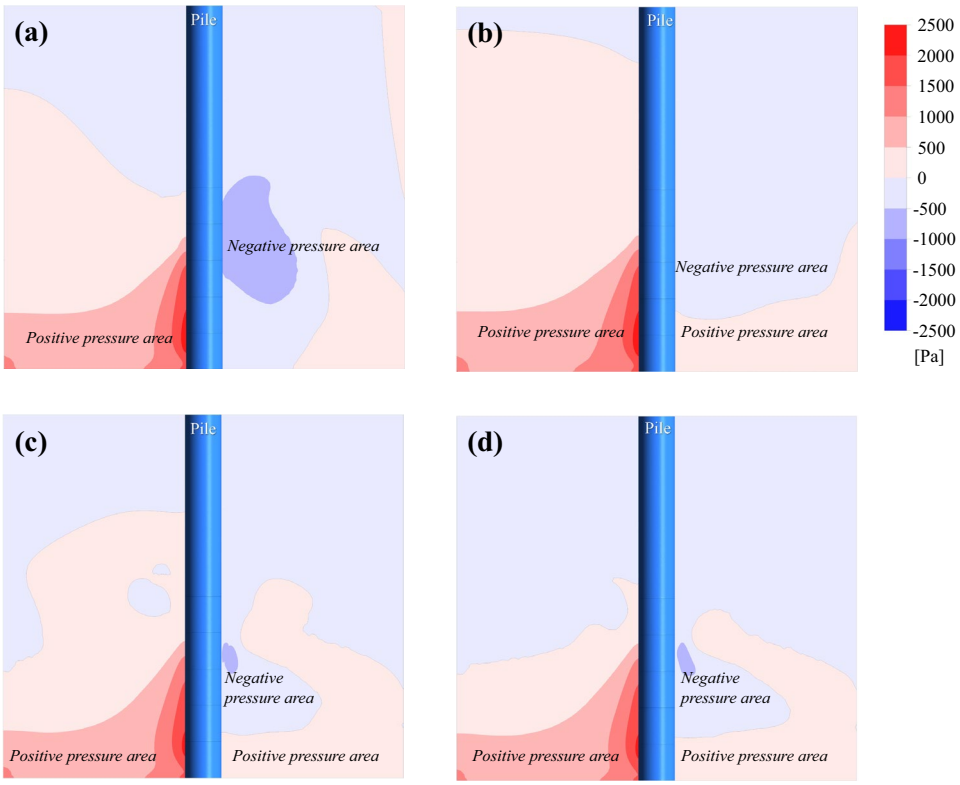

Fig. 12 Pressure difference distribution of profile $z=5.5D$ in Case 3D-5. **a** at $t=0.32$ s in Stage I; **b** at $t=0.4$ s in Stage II; **c** at $t=1$ s in Stage III; **d** at $t=2$ s in Stage III

overall trend, the action point gradually rises with increasing Reynolds number and impact velocity of submarine debris flow, and then stabilizes. However, the variation pattern of the action points depends on the configuration of numerical

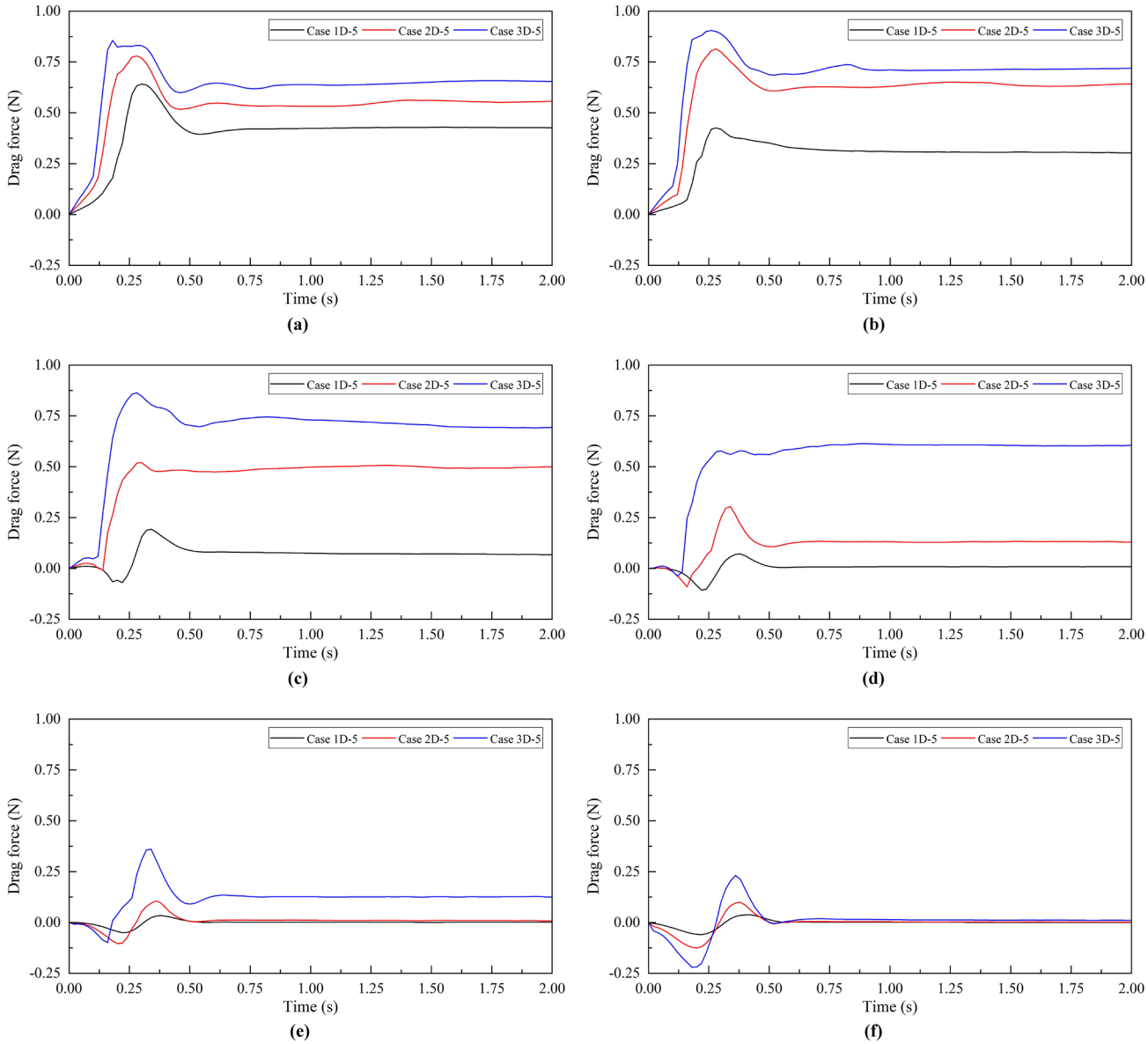

Fig. 13 Duration traces of the drag force for different pile units in cases 1D-5, 2D-5, and 3D-5. **a** H1 unit; **b** H2 unit; **c** H3 unit; **d** H4 unit; **e** H5 unit; **f** H6 unit

simulation conditions. We recommend conducting a more in-depth analysis of each condition. These findings offer valuable insights into when assessing the drag force exerted by submarine debris flows on piles.

4 Conclusions

The CFD approach for analyzing the effects of submarine debris flows on offshore wind turbine piles was applied and validated through a comparison with laboratory flume experiments. Subsequently, this approach was then used to explore the influence of submarine debris flows on piles across seven different Reynolds numbers, spanning from 9 to 710. The primary conclusions are as follows:

(1) Under the simulated conditions examined in this study, the vertical peak lift force constitutes only 2.1%–6.3% of the horizontal peak drag force. This observation underscores the primary importance of the drag force when considering the impact of debris flows on the pile. The notable disparity between the drag and lift force is due to the analysis model's constraint on flow velocity to the horizontal direction, resulting in minimal lift force on the pile. In future research endeavors involving more intricate scenarios, such as seabed sites

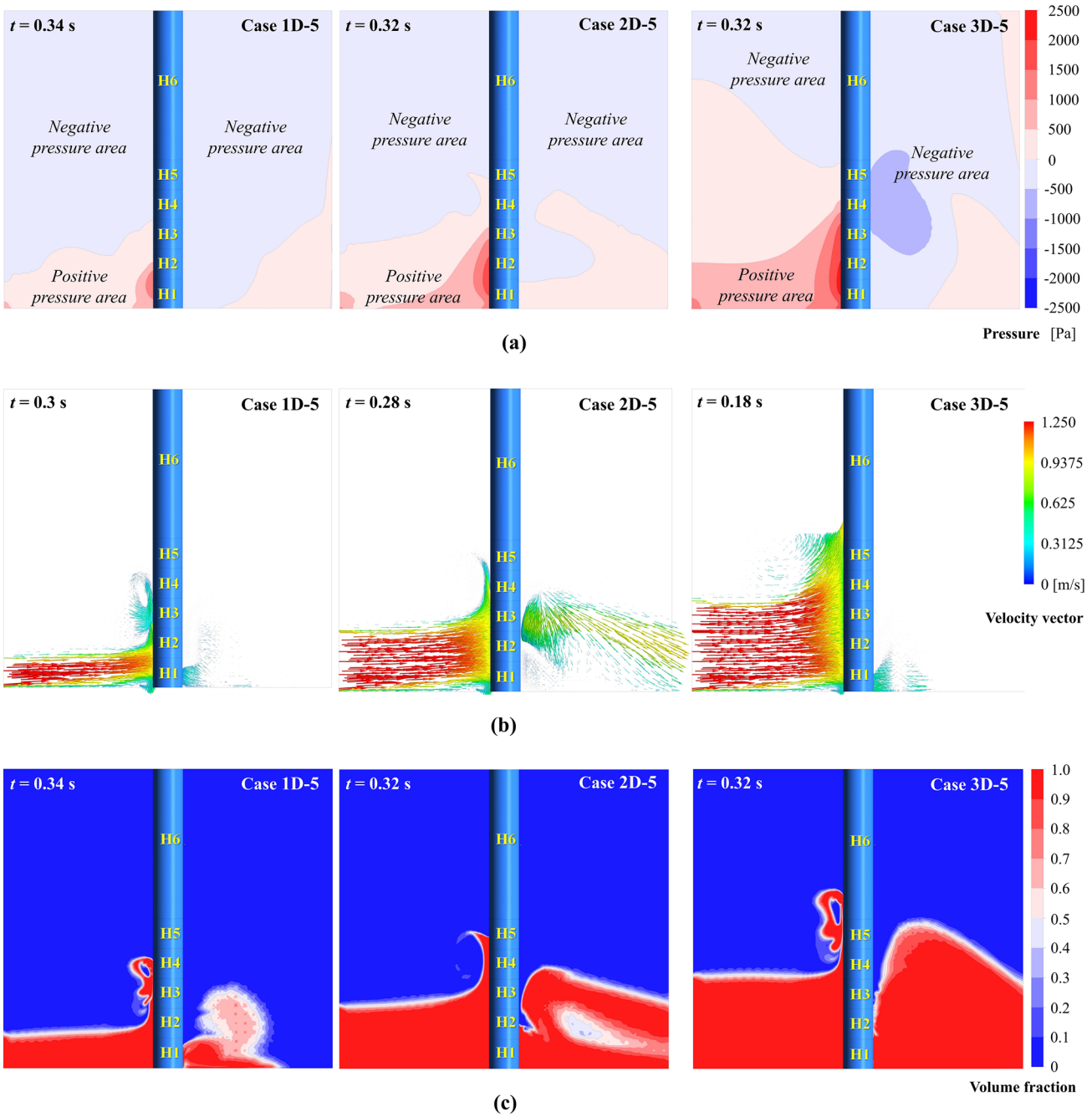

Fig. 14 Flow field distribution of profile $z = 5.5D$ in cases 1D-5, 2D-5, and 3D-5. **a** Pressure field around the pile; **b** Velocity vector around the pile; **c** Volume fraction of submarine debris flow

characterized by varying slopes, it will be imperative to focus on assessing the influence of the lift force.

(2) Based on the duration traces of the drag force exerted on the pile, this study divides the impact process into three stages for clarity. Notably, only stages I and III are observed in scenarios with low Reynolds numbers, shedding light on the mechanism governing the evolution of drag forces under varying Reynolds number conditions. It is worth highlighting that the peak drag force is as high as 1.6 times the stable drag force. Consequently, the peak drag force as the design reference value is recommended for assessing the impact load of submarine debris flows on piles.

(3) Within the conditions simulated in this study, the peak drag force caused by a large initial height of submarine debris flow reached approximately 3.4 times the

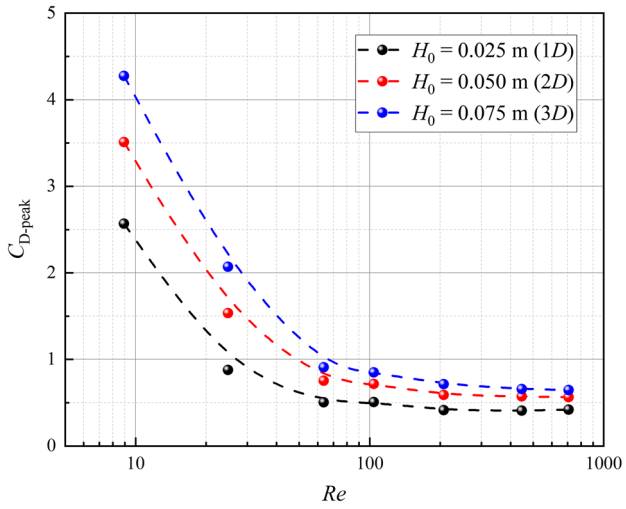

Fig. 15 Peak drag force coefficient as a function of Reynolds number under different initial heights of submarine debris flows

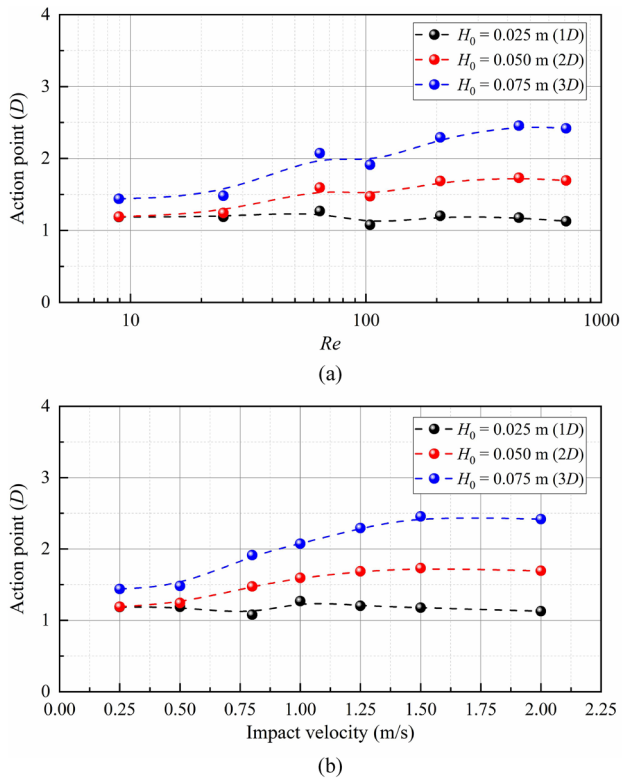

Fig. 16 Action point of the peak drag force as functions of **a** Re and **b** Impact velocity under different initial heights of submarine debris flows

smaller reference value. These disparities in the peak drag forces experienced by the pile, arising from differing initial heights of submarine debris flows, are conspicuously influenced by alterations in the flow dynamics occurring within the impact vicinity of the submarine debris flow. Moreover, the impact areas and the distribution of forces exerted on the pile vary significantly when dealing with differing initial flow heights. This nonuniform distribution of forces along the surface of the pile underscores the complexity of the interaction between the debris flow and the pile, highlighting the need for detailed future examination.

(4) The impact load inflicted by submarine debris flows upon the pile is notably influenced by several factors, including the dimensionless Reynolds number, the velocity, and density of the submarine debris flow, as well as the impact area of the submarine debris flow on the pile. One crucial aspect to consider is the determination of the action point of the drag force. Notably, the drag force coefficient exhibits a decline with increasing Reynolds number, eventually leveling off. In general, the action point first increases and then stabilizes with an increase in the impact velocity of the submarine debris flow and *Re*. These relationships were expressed roughly and quantitatively. Such findings offer valuable insights for the assessment of the impact force exerted by submarine debris flows on piles, providing essential insights for future evaluations in this context.

Acknowledgements Funding for the research has been supported by the National Natural Science Foundation of China (42277138 and 42207181), the Opening fund of State Key Laboratory of Ocean Engineering (GKZD010090), the European Commission (HORIZON MSCA-2024-PF-01, 101200637), the Fundamental Research Funds for the Central Universities (202441003), and the Shandong Province National-Level Leading Talent Supporting Project (2022GJJLJRC-15). This support is gratefully acknowledged.

Author contributions Xingsen Guo: Investigation, Methodology, Software, Visualization, Writing—Original Draft. Xiaolei Liu: Investigation, Conceptualization, Writing—Review & Editing. Hong Zhang: Writing—Review & Editing. Junkai Sun: Writing—Review & Editing. Thian Lai Goh: Writing—Review & Editing. Alessandro Leonardi: Writing—Review & Editing.

Data availability Data sharing is not applicable to this article as no new data were created or analyzed in this study.

Declarations

Conflict of interest The authors found no conflict of interest.

Open Access This article is licensed under a Creative Commons Attribution 4.0 International License, which permits use, sharing, adaptation, distribution and reproduction in any medium or format, as long as you give appropriate credit to the original author(s) and the source, provide a link to the Creative Commons licence, and indicate if changes were made. The images or other third party material in this article are included in the article's Creative Commons licence, unless indicated otherwise in a credit line to the material. If material is not included in the article's Creative Commons licence and your intended use is not permitted by statutory regulation or exceeds the permitted use, you will

need to obtain permission directly from the copyright holder. To view a copy of this licence, visit http://creativecommons.org/licenses/by/4.0/.

References

Byrne BW and Cassidy MJ (2002) Investigating the response of offshore foundations in soft clay soils. In: Proceedings of the 21st international conference on offshore mechanics and arctic engineering, 36142, 263–275. https://doi.org/10.1115/OMAE2002-28057

CFX (2020a) CFX solver models, CFX-program (Version 20.0) physical modelling documentation. Canonsburg, USA: ANSYS Inc

CFX (2020b) CFX solver theory, CFX-program (Version 20.0) theory documentation. Canonsburg, USA: ANSYS Inc

Dai PX, Nie J (2022) Robust expansion of extreme midlatitude storms under global warming. Geophys Res Lett 49(10):e2022GL099007. https://doi.org/10.1029/2022GL099007

Dong YK, Wang D, Randolph MF (2017) Investigation of impact forces on pipeline by submarine landslide using material point method. Ocean Eng 146:21–28. https://doi.org/10.1016/j.oceaneng.2017.09.008

Du X, Sun YF, Song YP, Xiu ZX (2020) Wave-induced liquefaction hazard assessment and liquefaction depth distribution: a case study in the Yellow River Estuary, China. IOP Conf Ser Earth Environ Sci 569:012011. https://doi.org/10.1088/1755-1315/569/1/012011

Dunnett S, Sorichetta A, Taylor G, Eigenbrod F (2020) Harmonised global datasets of wind and solar farm locations and power. Sci Data. https://doi.org/10.1038/s41597-020-0469-8

Faizi K, Faramarzi A, Dirar S, Chapman D (2019) Investigating the monotonic behaviour of hybrid tripod suction bucket foundations for offshore wind towers in sand. Appl Ocean Res 89:176–187. https://doi.org/10.1016/j.apor.2019.05.018

Fan N, Nian TK, Jiao HB, Jia YG (2018) Interaction between submarine landslides and suspended pipelines with a streamlined contour. Mar Georesour Geotechnol 36(6):652–662. https://doi.org/10.1080/1064119X.2017.1362084

Feng B, Sun HL, Cai YQ (2019) Experimental study of submarine landslide impact on offshore wind power piles. Ocean Eng 37(6):114–121. https://doi.org/10.16483/j.issn.1005-9865.2019.06.012

Gao FP, Yin ZY (2022) Instability and failure of subsea structures. J Marine Sci Eng 10(8):1001. https://doi.org/10.3390/jmse10081001

Guo XS, Liu XL, Luo QY, Chen BB, Zhang C (2022) Dimensional effect of CFD analysis for submarine landslides interactions with infinite suspension pipelines. Ocean Eng 266:113094. https://doi.org/10.1016/j.oceaneng.2022.113094

Guo XS, Fan N, Liu YH, Liu XL, Wang ZK, Xie XT, Jia YG (2023) Deep seabed mining: frontiers in engineering geology and environment. Int J Coal Scie Technol 10(1):23

Guo XS, Fan N, Zheng DF, Fu CW, Wu H, Zhang YJ, Song XL, Nian TK (2024a) Predicting impact forces on pipelines from deep-sea fluidized slides: a comprehensive review of key factors. Int J Min Sci Technol 34(2):211–225. https://doi.org/10.1016/j.ijmst.2024.02.001

Guo XS, Liu XL, Zheng TY, Zhang H, Lu Y, Li TT (2024b) A mass transfer-based LES modelling methodology for analyzing the movement of submarine sediment flows with extensive shear behavior. Coastal Eng 191:104531. https://doi.org/10.1016/j.coastaleng.2024.104531

Hance JJ (2003) Submarine slope stability. The University of Texas at Austin. https://www.bsee.gov/sites/bsee.gov/files/tap-technical-assessment-program/421ab.pdf

Haza ZF, Harahap ISH, Dakssa LM (2013) Experimental studies of the flow-front and drag forces exerted by subaqueous mudflow on inclined base. Nat Hazards 68(2):587–611. https://doi.org/10.1007/s11069-013-0643-9

Hsu SK, Kuo J, Lo CL, Tsai CH, Doo WB, Ku CY, Sibuet JC (2008) Turbidity currents, submarine landslides and the 2006 Pingtung earthquake off SW Taiwan. Terr Atmos Ocean Sci 19(6):767–772. https://doi.org/10.3319/TAO.2008.19.6.767(PT)

International Energy Agency (2021) Global Energy Review 2021. https://www.iea.org/reports/global-energy-review-2021/

Kirkwood PB (2016) Cyclic lateral loading of monopile foundations in sand. PhD thesis, University of Cambridge

Lai Y, Chen C, Yan ZZ, Zhu B (2024) The installation behavior and capacity of piggy-backed anchors for offshore wind turbine. Sustain Energy Technol Assess 70:103948. https://doi.org/10.1016/j.seta.2024.103948

Li RY, Chen JJ, Liao CC (2021) Numerical study on interaction between submarine landslides and a monopile using CFD techniques. J Marine Scie Eng 9(7):736. https://doi.org/10.3390/jmse9070736

Liu J, Tian JL, Yi P (2015) Impact forces of submarine landslides on offshore pipelines. Ocean Eng 95:116–127. https://doi.org/10.1016/j.oceaneng.2014.12.003

Liu XL, Wang YY, Zhang H, Guo XS (2023) Susceptibility of typical marine geological disasters: an overview. Geoenviron Disast 10:10. https://doi.org/10.1186/s40677-023-00237-6

Locat J, Lee HJ (2002) Submarine landslides: advances and challenges. Can Geotech J 39(1):193–212. https://doi.org/10.1139/t01-089

Melissas D and Asprogerakas E (2022). Spatial parameters for the development of floating wind farms in Greece. https://doi.org/10.48088/ejg.d.mel.13.4.001.017

Miceli F (2012) Offshore wind turbines foundation types. http://www.windfarmbop.com/tag/monopile/

Obelcz JB, Wood WT, Phrampus BJ, and Lee TR (2019) Nowcasting submarine slope instability at local, margin, and global scales using machine learning. Earth Arxiv. https://doi.org/10.31223/osf.io/ztq6f

Qian XS, Xu JP, Bai Y, Das HS (2020) Formation and estimation of peak impact force on suspended pipelines due to submarine debris flow. Ocean Eng 195:106695. https://doi.org/10.1016/j.oceaneng.2019.106695

Rui SJ, Zhang HJ, Xu H, Zha X, Xu MT, Shen KM (2024) Seabed structures and foundations related to deep-sea resource development: a review based on design and research. Deep Undergr Sci Eng 3(2):131–148. https://doi.org/10.1002/dug2.12042

Sahdi F, Gaudin C, Tom JG, Tong F (2019) Mechanisms of soil flow during submarine slide-pipe impact. Ocean Eng 186:106079. https://doi.org/10.1016/j.oceaneng.2019.05.061

Shan ZG, Wu H, Ni WD, Sun MJ, Wang KJ, Zhao LY, Lou YH, Liu A, Xie W, Zheng X, Guo XS (2022) Recent technological and methodological advances for the investigation of submarine landslides. J Marine Sci Eng 10(11):1728. https://doi.org/10.3390/jmse10111728

Shi J, Feng XB, Toumi R, Zhang C, Hodges KI, Tao A, Zhang W, Zheng JH (2024) Global increase in tropical cyclone ocean surface waves. Nat Commun 15(1):174. https://doi.org/10.1038/s41467-023-43532-4

Sørlie ER, Hartnik LO, Tran QA, Eiksund GR, Thakur V, Kjennbakken H, Degago S (2023) Physical model tests of clay-rich submarine landslides and resulting impact forces on offshore foundations. Ocean Eng 273:113966. https://doi.org/10.1016/j.oceaneng.2023.113966

Taftsoglou M, Valkaniotis S, Papathanassiou G, Klimis N, Dokas IM (2022) A detailed liquefaction susceptibility map of Nestos River Delta, Thrace, Greece based on surficial geology and

geomorphology. Geosciences 12:361. https://doi.org/10.3390/geosciences12100361

Wang LZ, Miao CZ (2008) Pressure on submarine pipelines under slowly sliding mud flows. Chin J Geotech Eng 30(7):982–987 (**in Chinese**)

Wang XF, Yang X, Zeng XW (2017) Lateral capacity assessment of offshore wind suction bucket foundation in clay via centrifuge modelling. J Renew Sustain Energy 9(3):595–593. https://doi.org/10.1063/1.4990831

Wang FW, Dai ZL, Nakahara Y, Sonoyama T (2018) Experimental study on impact behavior of submarine landslides on undersea communication cables. Ocean Eng 148:530–537. https://doi.org/10.1016/j.oceaneng.2017.11.050

Wang ZH, Zheng DF, Guo XS, Gu ZD, Shen YQ, Nian TK (2024) Investigation of offshore landslides impact on bucket foundations using a coupled SPH–FEM method. Geoenviron Disast 11:2. https://doi.org/10.1186/s40677-024-00266-9

Wind Europe (2020) Offshore Wind in Europe: Key Trends and Statistics 2019. https://windeurope.org/about-wind/statistics/offshore/european-offshore-wind-industry-keytrends-statistics-2019/

Wu XN, Hu Y, Li Y, Yang J, Duan L, Wang TG, Liao SJ (2019) Foundations of offshore wind turbines: a review. Renew Sustain Energy Rev 104:379–393. https://doi.org/10.1016/j.rser.2019.01.012

Wu H, Shi A, Ni WD, Zhao LY, Cheng ZC, Zhong QM (2024a) Numerical simulation on potential landslide–induced wave hazards by a novel hybrid method. Eng Geol 331:107429. https://doi.org/10.1016/j.enggeo.2024.107429

Wu TY, Zhang C, Guo XS (2024b) Dynamic responses of monopile offshore wind turbines in cold sea regions: ice and aerodynamic loads with soil-structure interaction. Ocean Eng 292:116536. https://doi.org/10.1016/j.oceaneng.2023.116536

Xu SM, Liu XL, Zhang C, Zhang H, Xie BT, Guo XS (2025) Numerical study on the stability of offshore pile-soil systems considering pore pressure response induced by extreme storms. Ocean Eng, 329:121178. https://doi.org/10.1016/j.oceaneng.2025.121178

Yu HY, Liu XL, Lu Y, Li WJ, Gao H, Wu RY, Li XY (2022) Characteristics of the sediment gravity flow triggered by wave-induced liquefaction on a sloping silty seabed: an experimental investigation. Front Earth Sci. https://doi.org/10.3389/feart.2022.909605

Zakeri A, Hawlader B (2013) Drag forces caused by submarine glide block or out-runner block impact on suspended (free-span) pipelines—numerical analysis. Ocean Eng 67:89–99. https://doi.org/10.1016/j.oceaneng.2013.03.007

Zakeri A, Høeg K, Nadim F (2008) Submarine debris flow impact on pipelines—Part I: experimental investigation. Coastal Eng 55(12):1209–1218. https://doi.org/10.1016/j.coastaleng.2008.06.003

Zakeri A, Høeg K, Nadim F (2009) Submarine debris flow impact on pipelines—Part II: numerical analysis. Coastal Eng 56(1):1–10. https://doi.org/10.1016/j.coastaleng.2008.06.005

Zakeri A, Hawlader B, Chi K (2012) Drag forces caused by submarine glide block or out-runner block impact on suspended (free-span) pipelines. Ocean Eng 47:50–57. https://doi.org/10.1016/j.oceaneng.2012.03.016

Zha X, Lai YQ, Rui SJ, Guo Z (2023) Fatigue life analysis of monopile-supported offshore wind turbines based on hyperplastic ratcheting model. Appl Ocean Res 136:103595. https://doi.org/10.1016/j.apor.2023.103595

Zhu CQ, Huang Y, Sun J (2020) Solid-like and liquid-like granular flows on inclined surfaces under vibration–Implications for earthquake-induced landslides. Comput Geotech 123:103598. https://doi.org/10.1016/j.compgeo.2020.103598

Publisher's Note Springer Nature remains neutral with regard to jurisdictional claims in published maps and institutional affiliations.